New Insights into the Vertical Structure of Clouds in Polar Lows, using Radar-Lidar Satellite Observations

Constantino Listowski, Mathias Rojo, Chantal Claud, Julien Delanoë, Jean-François Rysman, Quitterie Cazenave, G. Noer

Geophysical Research Letters

RESEARCH LETTER
10.1029/2020GL088785

New Insights Into the Vertical Structure of Clouds in Polar Lows, Using Radar-Lidar Satellite Observations

C. Listowski[1,2], M. Rojo[3], C. Claud[3], J. Delanoë[1], J.-F. Rysman[3], Q. Cazenave[1], and G. Noer[4]

[1]LATMOS/IPSL, UVSQ Université Paris-Saclay, UPMC Sorbonne Universités, CNRS, Guyancourt, France, [2]Now at CEA/DAM/DIF, F-91297 Arpajon, France, [3]LMD/IPSL, Ecole Polytechnique, IP Paris, ENS, PSL research University, Sorbonne University, CNRS, Palaiseau, France, [4]MET-Norway, Oslo, Norway

Key Points:
- Cloud top in polar lows reaches higher altitudes (~9 km) than commonly estimated so far (~5 km)
- Ice water content (IWC) and ice crystal effective radii are derived in 70 distinct polar lows, bringing strong constraints to modelers
- Spiraliform cloud features show larger IWCs than comma-shaped ones, in their upper part

Supporting Information:
- Supporting Information S1
- Figure S1
- Figure S2
- Figure S3
- Figure S4
- Figure S5
- Figure S6
- Figure S7
- Figure S8

Correspondence to:
C. Listowski and C. Claud,
constantino.listowski@cea.fr;
chantal.claud@lmd.polytechnique.fr

Citation:
Listowski, C., Rojo, M., Claud, C., Delanoë, J., Rysman, J.-F., Cazenave, Q., & Noer, G.(2020). New insights into the vertical structure of clouds in polar lows, using radar-lidar satellite observations. *Geophysical Research Letters*, *47*, e2020GL088785. https://doi.org/10.1029/2020GL088785

Received 8 MAY 2020
Accepted 8 JUL 2020
Accepted article online 29 JUL 2020

Abstract For the first time, we characterize the vertical distribution of cloud microphysical properties in polar lows (PLs). We base our investigation on colocations found between A-Train satellites overpasses and 82 PL occurrences evidenced from AVHRR observations in the Nordic Seas. We use the raDAR/liDAR DARDAR satellite cloud products to retrieve the thermodynamic phase and ice microphysical properties of clouds (ice water content [IWC] and ice crystal effective radius [r_{eff}]). Two thirds of the investigated PLs show cloud tops higher than commonly documented (5 km), and up to 9 km. PLs are largely dominated by the ice phase, with more supercooled liquid occurrences in the eye. We also show that spiraliform clouds have larger average IWC in the few kilometers below cloud top, by up to a factor of 2, compared to comma-shaped PLs.

Plain Language Summary Polar lows are intense maritime cyclones posing serious threats to mariners and coastal populations. Due to their limited size and sudden development, operational forecast struggles to correctly predict them. Additionally, the limited amount of observational constraints renders improvements of simulations difficult. We provide the first statistical analyses of cloud microphysical properties of these storms using radar and lidar satellite observations. We demonstrate much higher cloud tops than usually assumed. We highlight the cloud phase, describe the vertical distribution of ice mass and crystal size, and stress some differences between spiraliform and comma-shaped cyclones. These new constraints can be readily used to improve polar lows' simulations.

1. Introduction

During very intense cold air outbreaks, the Norwegian and Barents Seas are prone to the development of strong mesoscale cyclones called polar lows (PLs). These systems refer to maritime systems with near-surface winds exceeding 15 m s^{-1} (Heinemann & Claud, 1997; Rasmussen & Turner, 2003). This type of mesoscale cyclones may generate adverse weather and sea conditions (Rojo et al., 2019). There are different types of PLs. Some of them appear visually similar to tropical cyclones on satellite imagery with an eye-like feature (spiraliform cases), while some others have a comma cloud appearance (e.g., Carleton, 1995, 1996). Despite improving numerical weather prediction resources, PLs are still a challenge to forecast. The spatial positioning of these systems is currently the main shortcoming in the numerical weather prediction models. This is mainly due to their occurrence over data sparse areas and also their small size (150–600 km). Additionally, many aspects of the PLs are not well known (cloud height and cloud properties). These questions need to be addressed in order to make progress in our ability to make reliable forecasts for these fierce storms that pose serious threats to coastal areas and challenge numerical simulations (Stoll et al., 2020; Wu & Petty, 2010).

Spaceborne instruments are the primary tools used to observe PLs, but unlike tropical cyclones PLs are not routinely identified and tracked in real time. However, these systems can be manually identified. Rojo et al. (2019) subjectively tracked the full lifespan of PLs over a 20-year period (1999–2019), from genesis to dissipation, using the archive of the Advanced Very High Resolution Radiometer (AVHRR) thermal infrared Channel 4 (10.3–11.3 μm) images provided by the UK's Natural Environment Research Council to give the best estimated position of PL centers over the Nordic Seas. Since active remote sensing observations can be employed to characterize their vertical structure, as in recent case studies (Forsythe & Haynes, 2015; Sergeev

et al., 2017) using the cloud profiling radar (CPR) onboard CloudSat (Stephens et al., 2002, 2018), we matched all the PL tracks with coincident CloudSat-CALIPSO (Cloud Aerosol Lidar and Infrared Pathfinder Satellite Observations, Winker et al., 2010) tracks for the period 2006–2017. This way we have been able to characterize the cloud structure of PLs in terms of vertical extent, phase, and ice microphysical properties. Additionally, in forecasting, while the comma cloud is associated with a strong westerly component in the background flow, and the spiraliform is more associated with northerly to northeasterly flow, the two types are seen as parts of the same phenomena and are treated similarly. This paper also examines if there are further reasons to treat these two types of PLs differently.

2. Data and Methods

2.1. Colocation of PLs With A-Train Overpasses

The data set documented in Rojo et al. (2015) and Rojo, Noer, and Claud (2019) lists for each PL several characteristics like its formation stage (e.g., mature phase and decay), its shape (spiraliform, comma shaped, etc.), its diameter, and, when available, the minimum mean sea level pressure (mslp) constrained by in situ observation (see supporting information S1). Note that only the cloud vortex is included for calculating PL diameter; the cloud-band tails of comma-shaped systems are excluded from the analysis (Rojo et al., 2015; Rojo, Noer, & Claud, 2019).

For the colocation method used to find the overpasses crossing PL clouds identified by Rojo, Noer, and Claud (2019), a departure between the A-Train orbit and the AVHRR information used to detect the PL position of less than $\pm$30 min is required. This resulted in a total of 82 clear (non-tangent) coincidences for the period 2006–2017, for 70 distinct PLs (10 PLs are observed twice, and 2 PLs three times). Out of the 82 PLs' cloud covers overpassed by the A-Train, 70 of them were categorized as mature, 6 as in formation phase, and 6 in decay phase. Hence, any statistical investigation regarding the properties of PLs at different stage of their lives would not be conclusive. Also, because of the lack of conventional observations in the PLs' development areas, this classification relies on the appearance of cloud structures of PLs on satellite imagery. Therefore, the mature category, which groups observations when cloud structures of PLs are well organized, is relatively heterogeneous.

However, 27 PLs cloud features were unambiguously categorized as spiraliform and 38 as comma shaped. Other shapes displayed transition-like or undefined structures and were categorized as "other" in the present study. Based on the AVHRR images (e.g., Figure 1a), the cloud structures associated with the PLs have been identified to delimit the relevant part of the CloudSat satellite track where to look for the cloud top and to derive vertical profiles of microphysical properties (see supporting information S1). In addition to the cloud band clearly identified for any of the PL studied here, some satellite tracks also crossed the eye (36 out of 82) of the mesocyclone as well the other parts of the cloud band (32) (see Figure 1d).

2.2. Characterizing PLs With the DARDAR Products

The DARDAR products (Cazenave et al., 2019; Ceccaldi et al., 2013; Delanoë & Hogan, 2008, 2010) take advantage of the complimentary wavelengths of the CPR and the CALIOP (Cloud Aerosol Lidar with Orthogonal Polarization) lidar onboard CALIPSO to characterize hydrometeors in the atmosphere. Both satellites have been collecting collocated observations as part of the A-Train constellation (Stephens et al., 2002, 2018) since 2006. The 94-GHz CPR (3.2 mm) is more sensitive to the large ice and snow crystals and rain drops, while the lidar (532/1,064 nm) is much more sensitive to optically thin cirrus and cloud droplets. The DARDAR-MASK products (Ceccaldi et al., 2013; Delanoë & Hogan, 2010) have been used notably in the Arctic (Mioche et al., 2015) and the Antarctic (Listowski et al., 2019), respectively, to investigate cloud phase space-time distributions in polar regions. Both studies provide successful qualitative and quantitative comparisons to other data sets and ground-based measurements, demonstrating the robustness of these products. The DARDAR-CLOUD products (Cazenave et al., 2019; Delanoë & Hogan, 2010) provide ice water contents (IWCs) and ice crystal effective radius (r_{eff}). DARDAR-CLOUD was validated in the Arctic (Delanoë et al., 2013). An example of PL seen by the radar and the lidar as well as through the DARDAR products is shown in Figure 1.

In the Varcloud algorithm on which these products rely, the ice crystal mass-size relationship is critical (Cazenave et al., 2019; Delanoë et al., 2014). In order to evaluate the impact of the choice of the mass-size

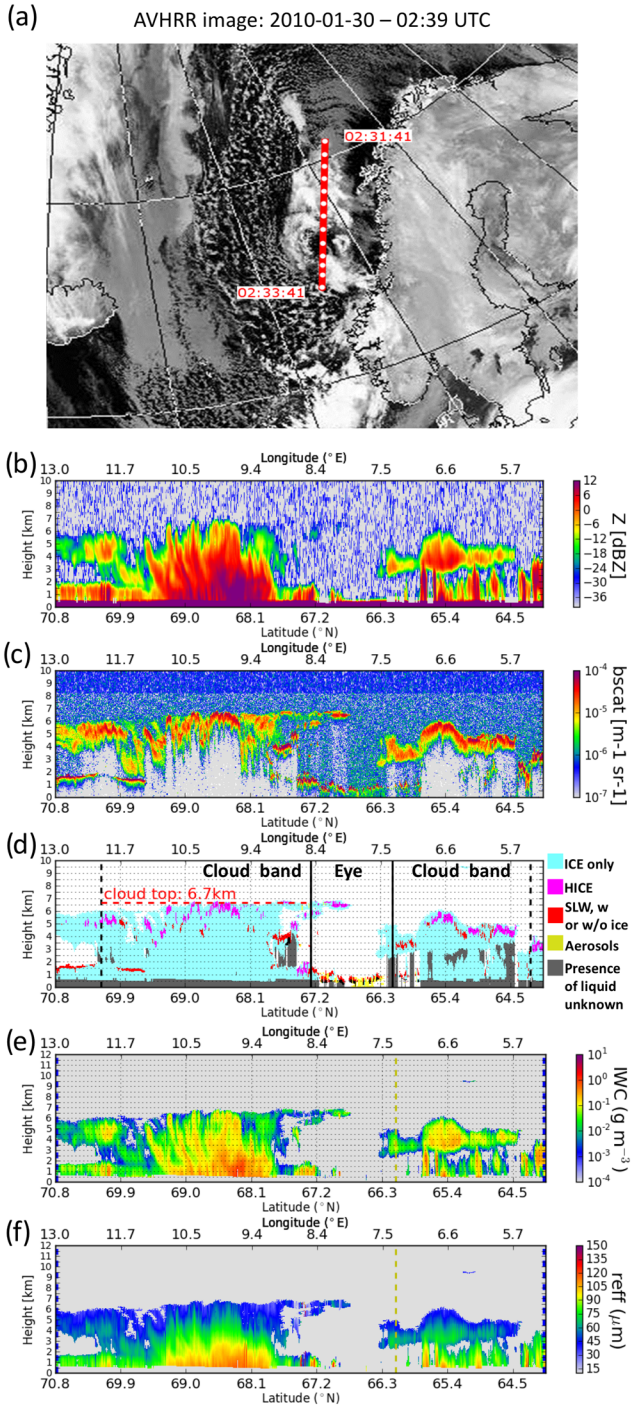

Figure 1. (a) AVHRR image of a polar low showing the CloudSat (A-Train) track (granule #19990), and the corresponding vertical transect of (b) the CPR reflectivity, (c) the CALIOP backscatter at 532 nm, (d) the DARDAR-MASK hydrometeor classification, (e) the DARDAR-CLOUD IWC (g m^{-3}), and (f) the DARDAR-CLOUD ice crystal effective radius (μm). For the DARDAR-MASK transect in (d) only the hydrometeor categories relevant to the present study are referenced, with Hice referring to the "highly concentrated ice category" (see text for details) and "SLW ..." gathering, for simplicity, instances of pure supercooled liquid water and mixed phase. Full description of the categories can be found in Ceccaldi et al. (2013), or Listowski et al. (2019) for a recent application to polar clouds.

relationship on the microphysical properties derived for PLs, we investigate two state-of-the-art mass-size relationships named the Brown and Francis Modified (BFM, Delanoë et al., 2014) and the composite (Cazenave et al., 2019) (see further details in supporting information S2).

3. Results: PLs Characteristics

3.1. Cloud Top Distribution

Figure 2a shows the cumulative distribution of cloud tops on a 500-m-binned scale for the three different categories of PL clouds investigated here (spiraliform, comma shaped, and other). Note that the PL cloud top is defined here as the maximum cloud height found across the PL cloud band and it is not a spatially averaged cloud top across the whole PL cloud structure (see supporting information Text S1). First, more than half of the PLs have cloud tops above 5 km, a value reported from case studies using CloudSat (Forsythe & Haynes, 2015; Sergeev et al., 2017). The sample cloud top average is 5.7 ± 1.4 km (one standard deviation). Second, based on our sample, comma-shaped clouds have on average a higher cloud top than the spiraliform ones (6.1 ± 1.4 km vs. 5.4 ± 1.3 km). This result is statistically significant at 95%. Also, 55% of spiraliform PL clouds have a cloud top above 5 km, while 79% of comma-shaped PL cloud features have a cloud top above 5 km.

Figure 2b shows the cloud top as a function of the PL diameter. The minimum mslp, when available, is color coded, while a gray square is used otherwise. Interestingly, there is a positive correlation between cloud top and diameter that although weak ($r = 0.36$) is statistically significant ($p < 0.999$). In other words, a PL with a larger diameter will tend to be associated with a higher cloud top. Also, the lower the minimum mslp (blue-red shaded color in Figure 2b), the higher the cloud tops, on average (see also supporting information Text S1 and Figure S1b).

3.2. Vertical Distributions of Cloud Phase and Ice Microphysical Properties

We focus on the cloud phase observed in PL clouds, separating cloud bands from the eye of the PL. The vertical profiles presented here are derived as explained in supporting information Text S3, with altitude given as the vertical distance to cloud top. Figure 3a shows the average phase composition of cloud bands in PLs, while Figure 3b shows the composition for clouds detected in the eye. In the cloud bands, the vast majority of the condensed phase is identified as ice (96% to 100% at each altitude level) and then 0–4% happen to be supercooled liquid water (SLW, Figure 3a). We also highlight an obvious feature within the ice phase, which stood out in the PL transects, namely, the higher presence of "highly concentrated ice" (hereafter referred to as Hice) in the first kilometers below cloud top (Figure 3a). In the upper 2 km of the PLs an increase in Hice is detected with a maximum at 23% close to cloud top. We recall here that this DARDAR category arises from high values of the lidar backscatter with no strong gradient in the lidar signal extinctions (as in SLW layers), or with temperatures below −40°C (Ceccaldi et al., 2013, and see Text S3). Hence, this observation may account for particular mechanisms happening near the top of PLs and involving high concentrations of small ice crystals. Very similar phase occurrences and vertical distributions are measured for spiraliform and comma-shaped clouds (not shown).

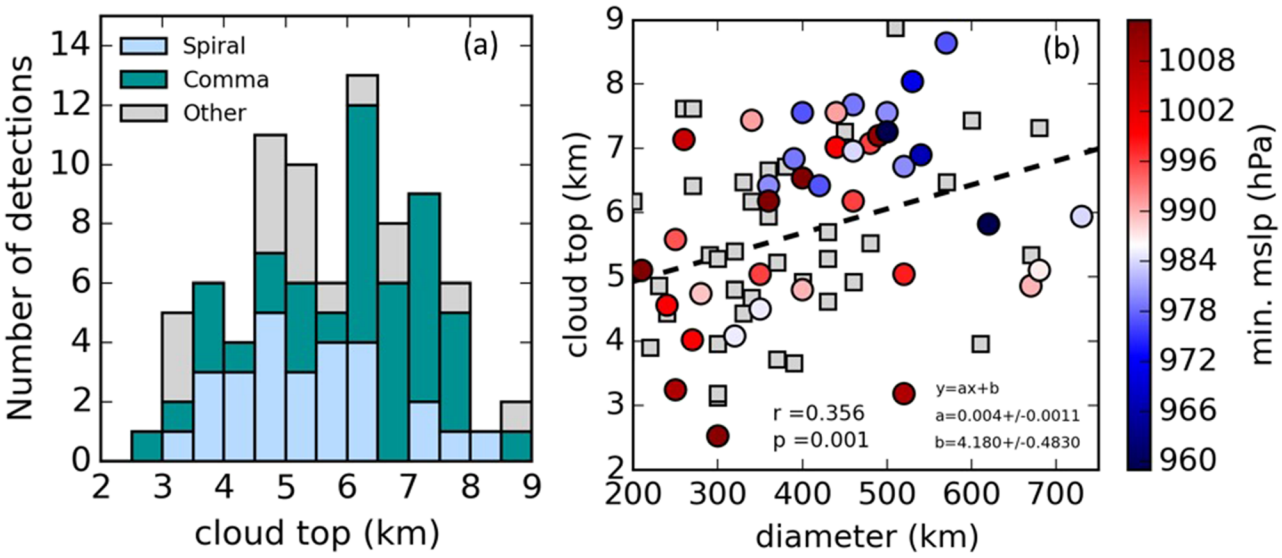

Figure 2. (a) Cumulative histograms of cloud tops recorded in polar lows (spiraliform, comma shaped, or other) expressed in km. (b) Cloud top plotted as a function of PL diameter. The color scale codes for the minimum surface pressure recorded in the PLs, when available. PLs with no pressure recorded are plotted with a gray square marker. A linear regression line is shown along with the Pearson correlation coefficient between both variables and the corresponding *p*-value.

In the eye, the average phase fractions are very different from what is observed in the cloud bands. The SLW fraction reaches higher values starting from 20% at ~1 km below cloud top and up to 60% closer to the surface. The ice fraction is correspondingly lower, and this illustrates the presence of shallow clouds with SLW in the eye (see section 4). Note that clouds from the delimited cloud bands may partly go over the eye (see Figure 1d, as an illustration of this), leading to non-zero ice fractions there.

In the following, we focus on the microphysical properties of the ice phase and investigate the vertical distribution of IWC and r_{eff}. As introduced in section 2.2, two mass-size relationships have been considered. Figures 4a and 4b (Figures S6a and S6b) show respectively the probability density function (pdf) of IWC and r_{eff} for the composite (BFM) mass-size relationship in all the PLs cloud bands regardless of altitude, between cloud top and the near-surface (prior to radar signal loss due to the ground clutter at about 0.5–1 km above the surface).

The IWC and r_{eff} distributions are almost identical whether considering only spiraliform or comma-shaped PL clouds, or all the PLs. Using the composite (BFM) mass-size relationship, the 25th and 75th percentiles of the IWC pdf are 0.013 (0.012) g m^{-3} and 0.13 (0.173) g m^{-3}, respectively, and the median is 0.044 (0.045) g m^{-3}. The 25th and 75th percentiles of the r_{eff} pdf are 48 (39) μm and 82 (73) μm, respectively, and the median is 63 (56) μm. Interestingly, the median IWC is the same for both mass-size relationships, and the difference is only significant for the 75th percentile, suggesting that the choice of the mass-size relationship essentially affects the largest values retrieved in PL clouds. All IWC and r_{eff} pdfs obtained for every single PL separately confirm this (see Figures S2 and S3, respectively).

Figures 4c and 4d show the average vertical profiles of IWC and r_{eff} in spiraliform, comma-shaped, and all PLs' clouds. The range of average IWC values goes from 0.02 (0.02) g m^{-3} at cloud top to 0.2 (0.5) g m^{-3} away from it, for the composite (BFM) law. The range of average r_{eff} values goes from 40 (30) μm at cloud top to 100 (80) μm away from it, for the composite (BFM) law.

There are noticeable differences between spiraliform and comma-shaped PLs in the first kilometers below cloud top (Figure 4c). IWC values reached in spiraliform PL clouds are between 20% and 100% higher than in comma-shaped PLs (see also Figure S7a). In other words, spiraliform PLs contain significantly larger IWCs than comma-shaped PLs in the area below cloud top. The average r_{eff} is also 15% to 20% larger (Figure S7b). Similar conclusions apply by using the BFM mass-size relationship (Figures S7c and S7d).

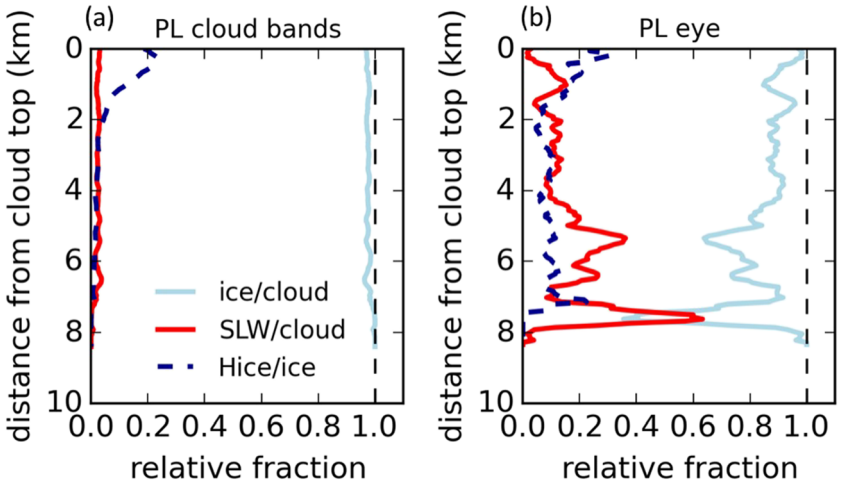

Figure 3. Vertical distribution of the relative occurrence (fraction) of the ice and supercooled liquid water in (a) the cloud bands and (b) the eye (when identified, see text for detail) as a function of distance to cloud top. The relative occurrence of highly concentrated ice crystals (Hice) with relation to the ice phase occurrence is also indicated (see text for details).

4. Discussion

In the past, in situ measurements have reported cloud top altitudes below 5 km and few events that have reached up to 7 km (e.g., Murakami, 2019; Sergeev et al., 2017). Here, we demonstrated that PLs with cloud top higher than 5 km are frequent, with events up to 9 km (Figure 2a). Additionally, at MET-Norway, cloud tops are, in an operational setting, determined by first reading off a calibrated cloud top temperature from infrared satellite images. This temperature is then compared to actual or prognostic soundings, to find the corresponding cloud height. For fully developed PLs, the vertical extent usually lies within the range 500–400 hPa. Interestingly, we report here 21 PLs out of 82 with cloud tops above 400 hPa and up to 250–300 hPa (Figure S1a). It must be stressed that the CloudSat/CALIPSO sampling gives a space-time snapshot of the vertical structure of each PL and does not allow to capture neither the full horizontal span nor the full lifetime of the PL clouds. Thus, we may miss the highest part of any given PL because it is outside the field of view or because it has not formed yet. However, this limitation does not impact our main conclusion that cloud top in PLs reaches higher altitudes than commonly estimated so far.

In the forecasting community at MET-Norway, the formation of both shallow and deep individual convection cells in the eye is often seen as a first sign of dissipation; the eye is usually dry in a developing PL, and these cells happen typically in the latter part of the life cycle. Being "younger", they are expected to have more supercooled droplets than the older and larger glaciated cloud bands around the center. Interestingly, this is in line with our findings of larger relative occurrences of SLW in the eye of the PL (Figure 3b).

Using two distinct mass-size relationships brings more confidence to the results presented here, especially since the use of distinct relationships does not impact, for instance, the median value of IWC $= 0.045$ g m^{-3} across all PLs (section 3.2). Interestingly, considering the median IWC in each of the PLs separately leads to very similar distributions of the values across the PL sample, with both relationships (Figures S8a and S8b), while the IWC 99th percentiles differ much more (Figures S8c and S8d), demonstrating that the choice of the mass-size relationship will mainly affect the retrieved largest values that may be reached by IWC (on the order of 1 g m^{-3}).

Distinguishing between spiraliform and comma-shaped structures, we showed that the latter tend to top at higher altitudes on average, while they reach lower IWC by a factor of up to 2 in their upper part and near cloud top, with slightly smaller crystals (by 15–20%). This is very likely related to the underlying mechanisms causing the formation and, or, intensification of these mesocyclones where latent heating remains a major driver of their amplitude (e.g., Claud et al., 2004; McInnes et al., 2011). For instance, it has been suggested

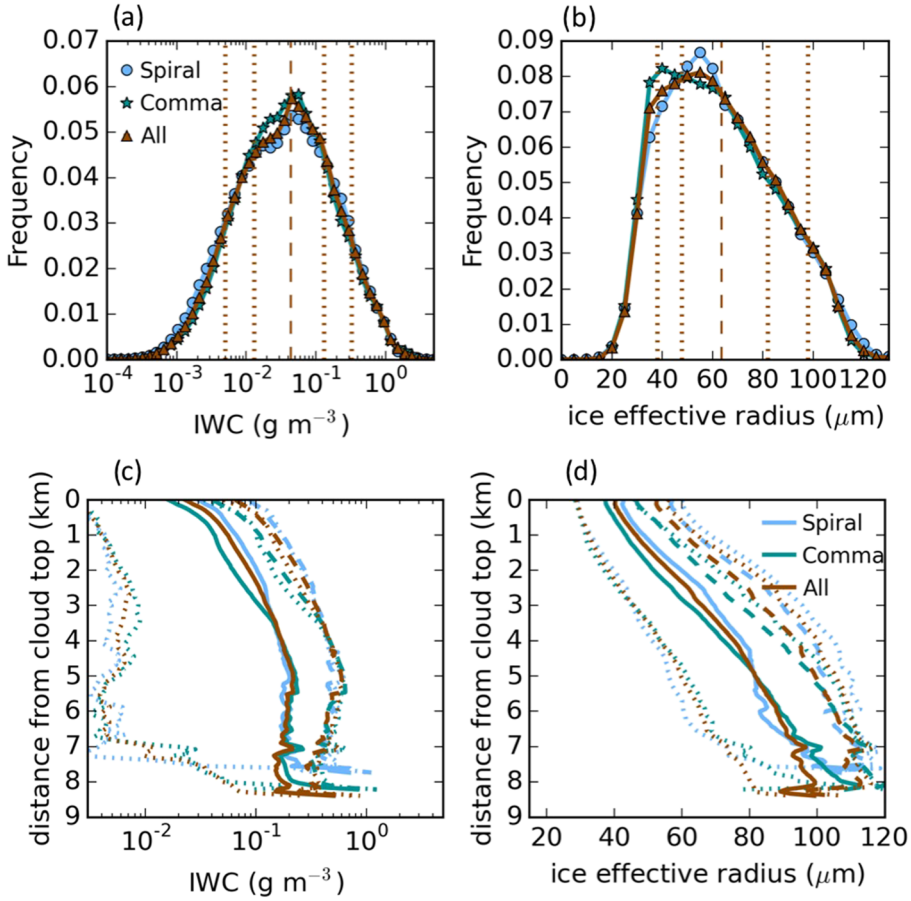

Figure 4. Probability density function of (a) IWC values and (b) r_{eff} values in PLs using the composite mass-size relationship. The vertical dotted lines represent the 10th, 25th, 75th, and 95th percentiles of the values distributions across all PLs, while the dashed line is the median (see text for the numerical values). (c, d) Vertical profiles of average (c) IWC and (d) r_{eff}. The blue, green, and brown colors code for spiraliform, comma-shaped, and all PLs, respectively. The dashed lines represent the average value plus standard deviation, while the dotted lines represent the 10th and 90th percentiles of the values distributions. (See Figure S6 for similar plots using the alternate BFM mass-diameter law.)

that both types of PLs may be related to distinct dynamical pathways, although no consensus exists today (Rasmussen & Turner, 2003). In any case, this framework leads to suggest that spiraliform cloud structures host enhanced latent heating due to the larger IWC and/or more numerous and larger crystals because of stronger updraughts maintained by a more vigorous convection. Moreover, we can speculate that the highly concentrated ice crystals observed at the top of PLs may be indicative of ascending winds which would maintain and, or, cause the formation of highly concentrated small ice crystals (seen by the lidar only). This point may be related to the possible generation of secondary ice crystals upon collision of graupels with smaller ice crystals in convective clouds (Field et al., 2017; Takahashi et al., 1995; Yano & Phillips, 2011). This, however, remains to be investigated through detailed modeling of ice cloud formation within PLs.

Given the importance of latent heating in PLs amplitude, we investigated possible links between IWC and the minimum pressure recorded at the surface as a signature of the mesocyclone strength. In theory larger IWC should come along with larger latent heating, hence more advection of higher vorticity air masses from the upper atmosphere with increased surface winds as a result. A weak correlation arises between the 99th percentile of the IWC distribution in the PLs and the recorded surface pressure (not shown), however in a non-significant way (p-values > 0.1), and the correlation gets even worse when considering wind speed values (when available). The reduced PL sample, which is considered when focusing on information of wind

speed, and the nature of the wind estimation itself make it very difficult to link cloud properties and in situ dynamics any further for the present study.

5. Conclusions

The synergistic raDAR-liDAR (DARDAR) satellite cloud products were used in this study to investigate the vertical distribution of microphysical properties of clouds associated with PLs between December 2006 and April 2017, in the Nordic Seas. The DARDAR-MASK product was used to investigate the cloud top and the thermodynamical phase of the clouds, while the DARDAR-CLOUD provided the IWC and r_{eff}. We used two mass-size relationships for comparison purpose and to provide modelers with a more reliable range of possible IWC and r_{eff} values, given that no extensive in situ data sets exist, which could guide in the best mass-size relationship to use for PLs' clouds. Our conclusions can be summarized as follows:

1. Cloud top in PLs reaches higher altitudes (~9 km) than commonly estimated so far (~5 km). The average PL cloud top is 5.7 ± 1.4 km (one standard deviation). In our sample, spiraliform cloud features have an average cloud top at 5.4 ± 1.3 km, while for comma-shaped clouds it is 6.1 ± 1.4 km.
2. There is a significant trend relating cloud top altitude to PL diameter, with consistently lower surface pressures measured for the higher (and larger) mesocyclones.
3. The ice phase is dominant in the cloud bands with an average of 96% to 100% of the total cloud pixels being identified as ice. SLW is much more abundant in the eye (20–60% of the total cloud pixels).
4. The median value of IWC in PLs is the same whatever the mass-size relationship used: 0.045 g m^{-3}. The range of average IWC values goes from 0.02 (0.02) g m^{-3} at cloud top to 0.2 (0.5) g m^{-3} away from it, for the composite (BFM) law.
5. The median r_{eff} value is 63 (56) μm for the composite (BFM) law. The range of average r_{eff} values goes from 40 (30) μm at cloud top to 100 (80) μm away from it, for the composite (BFM) law.
6. Spiraliform PL clouds display larger IWCs in the few (~3) kilometers below cloud top by up to a factor of 1.8–2, compared to comma-shaped cloud features, and 15–20% larger ice crystals. There, both PL types display larger contributions of the highly concentrated ice crystals to the ice phase.

The limitation of the present study lies in the partial space and time sampling of the PLs related to the limited field of view of the radar and the lidar onboard polar orbiters. However, modeling experiments can use these constraints to improve our understanding of the underlying microphysics and dynamical pathways at play across the full PL cloud structures.

Data Availability Statement

The data used in this study are available online (at https://www.icare.univ-lille.fr/archive?dir=CLOUDSAT/DARDAR-SUBSET/Listowski-et-al_2020_Polarlows/).

Acknowledgments

We thank the Aeris/ICARE data infrastructure for providing access to the DARDAR-MASK products (https://www.icare.univ-lille.fr/, last access: July 2019) and Nicolas Pascal for his assistance in the project. We thank the NASA CloudSat Project and NASA/LaRC/ASDC for the CloudSat and CALIPSO products. This work was partially supported by the National Center of Spatial Studies (CNES) program EECLAT (Expecting EarthCare, Learning from A-Train).

References

Carleton, A. M. (1995). On the interpretation and classification of mesoscale cyclones from satellite IR imagery. *International Journal of Remote Sensing*, *16*(13), 2457–2485. https://doi.org/10.1080/01431169508954569

Carleton, A. M. (1996). Satellite climatological aspects of cold air mesocyclones in the Arctic and Antarctic. *Global Atmosphere and Ocean System*, *5*(1), 1–42.

Cazenave, Q., Ceccaldi, M., Delanoë, J., Pelon, J., Groß, S., & Heymsfield, A. (2019). Evolution of DARDAR-CLOUD ice cloud retrievals: New parameters and impacts on the retrieved microphysical properties. *Atmospheric Measurement Techniques*, *12*, 2819–2835. https://doi.org/10.5194/amt-12-2819-2019

Ceccaldi, M., Delanoë, J., Hogan, R. J., Pounder, N. L., Protat, A., & Pelon, J. (2013). From CloudSat-CALIPSO to EarthCare: Evolution of the DARDAR cloud classification and its comparison to airborne radar-lidar observations. *Journal of Geophysical Research: Atmospheres*, *118*, 7962–7981. https://doi.org/10.1002/jgrd.50579

Claud, C., Heinemann, G., Raustein, E., & McMurdie, L. (2004). Polar low le Cygne: Satellite observations and numerical simulations. *Quarterly Journal of the Royal Meteorological Society*, *130*(598), 1075–1102. https://doi.org/10.1256/qj.03.72

Delanoë, J., & Hogan, R. J. (2008). A variational scheme for retrieving ice cloud properties from combined radar, lidar, and infrared radiometer. *Journal of Geophysical Research*, *113*, D07204. https://doi.org/10.1029/2007jd009000

Delanoë, J., & Hogan, R. J. (2010). Combined CloudSat-CALIPSO-MODIS retrievals of the properties of ice clouds. *Journal of Geophysical Research*, *115*, D00H29. https://doi.org/10.1029/2009jd012346

Delanoë, J. M. E., Heymsfield, A. J., Protat, A., Bansemer, A., & Hogan, R. J. (2014). Normalised particle size distribution for remote sensing application. *Journal of Geophysical Research: Atmospheres*, *119*, 4204–4227. https://doi.org/10.1002/2013JD020700

Delanoë, J., Protat, A., Jourdan, O., Pelon, J., Papazzoni, M., Dupuy, R., Gayet, J., & Jouan, C. (2013). Comparison of Airborne In Situ, Airborne Radar–Lidar, and Spaceborne Radar–Lidar Retrievals of Polar Ice Cloud Properties Sampled during the POLARCAT Campaign. *Journal of Atmospheric and Oceanic Technology*, *30*, 57–73. https://doi.org/10.1175/JTECH-D-11-00200.1

Field, P. R., Lawson, R. P., Brown, P. R. A., Lloyd, G., Westbrook, C., Moisseev, D., et al. (2017). Secondary ice production: Current state of the science and recommendations for the future. *Meteorological Monographs*, *58*, 7.1–7.20. https://doi.org/10.1175/AMSMONOGRAPH-S-D-16-0014.1

Forsythe, J. M., & Haynes, J. M. (2015). CloudSat observes a Labrador Sea polar low. *Bulletin of the American Meteorological Society*, *96*, 1229–1231. https://doi.org/10.1175/BAMS-D-14-00058.1

Heinemann, G., & Claud, C. (1997). Report of a workshop on "theoretical and observational studies of polar lows" of the European Geophysical Society Polar Lows Working Group. *Bulletin of the American Meteorological Society*, *78*(11), 2643–2658. https://doi.org/10.1175/1520-0477-78.11.2643

Listowski, C., Delanoë, J., Kirchgaessner, A., Lachlan-Cope, T., & King, J. (2019). Antarctic clouds, supercooled liquid water and mixed phase, investigated with DARDAR: Geographical and seasonal variations. *Atmospheric Chemistry and Physics*, *19*, 6771–6808. https://doi.org/10.5194/acp-19-6771-2019

McInnes, H., Kristiansen, J., Kristjánsson, J. E., & Schyberg, H. (2011). The role of horizontal resolution for polar low simulations. *Quarterly Journal of the Royal Meteorological Society*, *137*(660), 1674–1687. https://doi.org/10.1002/qj.849

Mioche, G., Jourdan, O., Ceccaldi, M., & Delanoë, J. (2015). Variability of mixed-phase clouds in the Arctic with a focus on the Svalbard region: A study based on spaceborne active remote sensing. *Atmospheric Chemistry and Physics*, *15*, 2445–2461. https://doi.org/10.5194/acp-15-2445-2015

Murakami, M. (2019). Inner structures of snow clouds over the Sea of Japan observed by instrumented aircraft: A review. *Journal of the Meteorological Society of Japan. Ser. II*, *97*(1), 5–38, Released February 14, 2019. https://doi.org/10.2151/jmsj.2019-009

Rasmussen, E. A., & Turner, J. (2003). Introduction. In *Polar lows: Mesoscale weather systems in the polar regions* (pp. 1–51). Cambridge: Cambridge University Press.

Rojo, M., Claud, C., Mallet, P.-E., Noer, G., Carleton, A. M., & Vicomte, M. (2015). Polar low tracks over the Nordic Seas: A 14-winter climatic analysis. *Tellus*, *67*(1). https://doi.org/10.3402/tellusa.v67.24660

Rojo, M., Claud, C., Noer, G., & Carleton, A. M. (2019). In situ measurements of surface winds, waves, and sea state in polar lows over the North Atlantic. *Journal of Geophysical Research: Atmospheres*, *124*, 700–718. https://doi.org/10.1029/2017JD028079

Rojo, M., Noer, G., & Claud, C. (2019). Polar low tracks in the Norwegian Sea and the Barents Sea from 1999 until 2019. *PANGAEA*. https://doi.org/10.1594/PANGAEA.903058

Sergeev, D. E., Renfrew, I. A., Spengler, T., & Dorling, S. R. (2017). Structure of a shear-line polar low. *Quarterly Journal of the Royal Meteorological Society*, *143*, 12–26. https://doi.org/10.1002/qj.2911

Stephens, G., Winker, D., Pelon, J., Trepte, C., Vane, D., Yuhas, C., et al. (2018). CloudSat and CALIPSO within the A-Train: Ten years of actively observing the Earth system. *Bulletin of the American Meteorological Society*, *99*, 569–581. https://doi.org/10.1175/BAMS-D-16-0324.1

Stephens, G. L., Vane, D. G., Boain, R. J., Mace, G. G., Sassen, K., Wang, Z., et al. (2002). The CloudSat mission and the A-Train. *Bulletin of the American Meteorological Society*, *83*, 1771–1790. https://doi.org/10.1175/bams-83-12-1771

Stoll, P. J., Valkonen, T. M., Graversen, R. G., & Noer, G. (2020). A well-observed polar low analysed with a regional and a global weather-prediction model. *Quarterly Journal of the Royal Meteorological Society*, 1–28. https://doi.org/10.1002/qj.3764

Takahashi, T., Nagao, Y., & Kushiyama, Y. (1995). Possible high ice particle production during graupel–graupel collisions. *Journal of the Atmospheric Sciences*, *52*(24), 4523–4527. doi:10.1175/1520-0469(1995)052<4523:PHIPPD>2.0.CO;2

Winker, D. M., Pelon, J., Coakley, J. A., Ackerman, S. A., Charlson, R. J., Colarco, P. R., et al. (2010). The CALIPSO mission. *Bulletin of the American Meteorological Society*, *91*, 1211–1230. https://doi.org/10.1175/2010BAMS3009.1

Wu, L., & Petty, G. W. (2010). Intercomparison of bulk microphysics schemes in model simulations of polar lows. *Monthly Weather Review*, *138*, 2211–2228. https://doi.org/10.1175/2010MWR3122.1

Yano, J.-I., & Phillips, V. T. J. (2011). Ice–ice collisions: An ice multiplication process in atmospheric clouds. *Journal of the Atmospheric Sciences*, *68*, 322–333. https://doi.org/10.1175/2010JAS3607.1

References From the Supporting Information

Brown, P. R. A., & Francis, P. N. (1995). Improved measurements of the ice water content in cirrus using a total–water probe. *Journal of Atmospheric and Oceanic Technology*, *12*, 410–414. DOI: 10.1175/1520-0426(1995)012<0410:IMOTIW>2.0.CO;2

Ceccaldi, M. (2014). Combinaison de mesures actives et passives pour l'étude des nuages dans le cadre de la préparation à la mission EarthCARE, Climatologie, PhD thesis, Universite de Versailles Saint-Quentin-en-Yvelines, available at: https://hal. archives-ouvertes. fr/tel-01119939 (last access: July 2019).

Dezitter, F., Grandin, A., Brenguier, J.-L., Hervy, F., Schlager, H., Villedieu, P., & Zalamansky, G. (2013). HAIC—High altitude ice crystals. Paper presented at 5th AIAA Atmospheric and Space Environments Conference.

Heymsfield, A. J., Schmitt, C., Bansemer, A., & Twohy, C. H. (2010). Improved representation of ice particle masses based on observations in natural clouds. *Journal of the Atmospheric Sciences*, *67*(10), 3303–3318. https://doi.org/10.1175/2010JAS3507.1

Hogan, R. J., Illingworth, A. J., O'Connor, E. J., & Poiares Baptista, J. P. V. (2003). Characteristics of mixed-phase clouds. II: A climatology from ground-based lidar. *Quarterly Journal of the Royal Meteorological Society*, *129*(592), 2117–2134. https://doi.org/10.1256/qj.01.209